(movie S11) were unable to produce substantial emission (fig. S9A), indicating that the scenario is coherent. Thus, our hydrodynamic simulations show that the hot and bright impacts after the eruption are caused by the high density (>>10^{10} cm^{-3}) and speed (free-fall speed, 300 to 450 km/s) of the downfalling debris. These values are close to those of the plasma involved in stellar accretion flows.

For most stellar accretion flows [see (*15*) for an exception], the mass accretion rates derived from x-rays are consistently lower (by one or more orders of magnitude) than the corresponding rates derived from UV–optical–near infrared observations (*24*–*26*). According to our analysis of a solar event, the impact of the dense fragments leads to detectable high-energy emission. From the model, we find that the mass of plasma responsible for the brightenings in the 171 Å channel (see supplementary materials, section S3) ranges between 5 and 30% of the original mass of the fragments. This is mainly because of the absorption by the optically thick chromosphere and/or by the dense part of the material outflowing after the impact (depending on the orientation of the impact region with respect to the line of sight). In addition, the simulations tell us that droplets with low density or low velocity are unable to produce substantial emission; the observations tell us that some of the falling fragments produce no detectable brightening. Therefore, both the absorption of x-ray emission from dense plasma and the wide range of velocity and density values of the infalling fragments contribute to underestimating the mass accretion rate from the XUV band.

Our simulations also show that the XUV emission arises from the original impacting material. Although our fragmented solar downflows differ from the conceptual stellar accretion flows (which are hypothesized to be continuous streams, channeled by the magnetic field), the structure of the impact region (presenting hot plasma partially rooted in the chromosphere) is similar in the two cases. Moreover, as suggested recently (*19*), the accretion flows are likely to be frayed, even when they are magnetically confined and stream along straight tubes. Therefore, the dynamics and energetics spatially resolved in the solar observations are a template and laboratory to study accretion processes in astrophysics.

References and Notes

1. D. Lynden-Bell, J. E. Pringle, *Mon. Not. R. Astron. Soc.* **168**, 603–637 (1974).
2. L. Hartmann, *Accretion Processes in Star Formation*, Cambridge Astrophysics Series (Cambridge Univ. Press, New York, 1998).
3. A. Koenigl, *Astrophys. J.* **370**, L39–L43 (1991).
4. C. Bertout, G. Basri, J. Bouvier, *Astrophys. J.* **330**, 350–373 (1988).
5. A. Natta, L. Testi, S. Randich, *Astron. Astrophys.* **452**, 245–252 (2006).
6. G. J. Herczeg, L. A. Hillenbrand, *Astrophys. J.* **681**, 594–625 (2008).
7. J. H. Kastner, D. P. Huenemoerder, N. S. Schulz, C. R. Canizares, D. A. Weintraub, *Astrophys. J.* **567**, 434–440 (2002).
8. A. Telleschi, M. Güdel, K. R. Briggs, M. Audard, L. Scelsi, *Astron. Astrophys.* **468**, 443–462 (2007).
9. C. Argiroffi, A. Maggio, G. Peres, *Astron. Astrophys.* **465**, L5–L8 (2007).
10. J.-F. Donati *et al.*, *Mon. Not. R. Astron. Soc.* **386**, 1234–1251 (2008).
11. J. J. Drake, *13th Cambridge Workshop on Cool Stars, Stellar Systems and the Sun*, vol. 560 of *ESA Special Publication*, F. Favata, G. A. J. Hussain, B. Battrick, Eds. (European Space Agency, Noordwijk, 2005), p. 519.
12. H. M. Günther, J. H. M. M. Schmitt, J. Robrade, C. Liefke, *Astron. Astrophys.* **466**, 1111–1121 (2007).
13. G. G. Sacco *et al.*, *Astron. Astrophys.* **522**, A55 (2010).
14. S. Orlando *et al.*, *Astron. Astrophys.* **510**, A71 (2010).
15. N. S. Brickhouse, S. R. Cranmer, A. K. Dupree, G. J. M. Luna, S. Wolk, *Astrophys. J.* **710**, 1835–1847 (2010).
16. A. K. Dupree *et al.*, *Astrophys. J.* **750**, 73 (2012).
17. J. R. Lemen *et al.*, *Sol. Phys.* **275**, 17–40 (2012).
18. W. D. Pesnell, B. J. Thompson, P. C. Chamberlin, *Sol. Phys.* **275**, 3–15 (2012).
19. D. E. Innes, R. H. Cameron, L. Fletcher, B. Inhester, S. K. Solanki, *Astron. Astrophys.* **540**, L10 (2012).
20. X. Cheng *et al.*, *Astrophys. J.* **745**, L5 (2012).
21. G. E. Brueckner *et al.*, *Sol. Phys.* **162**, 357–402 (1995).
22. J.-P. Wuelser *et al.*, *Society of Photo-Optical Instrumentation Engineers (SPIE) Conference Series*, S. Fineschi, M. A. Gummin, Eds. (SPIE, San Diego, 2004), vol. 5171, pp. 111–122.
23. N. Calvet, E. Gullbring, *Astrophys. J.* **509**, 802–818 (1998).
24. E. Gullbring, L. Hartmann, C. Briceno, N. Calvet, *Astrophys. J.* **492**, 323–341 (1998).
25. J. Muzerolle, N. Calvet, C. Briceño, L. Hartmann, L. Hillenbrand, *Astrophys. J.* **535**, L47–L50 (2000).
26. R. L. Curran *et al.*, *Astron. Astrophys.* **526**, A104 (2011).

Acknowledgments: We thank B. De Pontieu for help and suggestions. F.R., G.P., and S.O. acknowledge support from Italian Ministero dell'Università e Ricerca and Agenzia Spaziale Italiana, contract I/023/09/0. P.T. was supported by contract SP02H1701R from Lockheed-Martin to the Smithsonian Astrophysical Observatory. P.T. and C.J.S. are supported by NASA contract NNG04EA00C for the SDO AIA. E.L. is supported by NASA grants NNX11AC20G and NNX10AQ58G and NSF grant AGS-1154443. S.O. acknowledges partial support from the INAF. The software used in this work was, in part, developed by the U.S. Department of Energy–supported Advanced Simulation and Computing/Alliance Center for Astrophysical Thermonuclear Flashes at the University of Chicago. We acknowledge the CINECA Award HP10CEG9MW and INAF/Osservatorio Astronomico di Palermo for high-performance computing resources and support. SDO data were supplied courtesy of the SDO/HMI and SDO/AIA consortia. SDO is the first mission to be launched for NASA's Living With a Star Program. See the supplementary materials for details on the data, data analysis, and modeling.

Supplementary Materials

www.sciencemag.org/cgi/content/full/science.1235692/DC1
Materials and Methods
Supplementary Text
Figs. S1 to S9
Table S1
References (*27*–*40*)
Movies S1 to S18

28 January 2013; accepted 5 June 2013
Published online 20 June 2013;
10.1126/science.1235692

Switchable Static and Dynamic Self-Assembly of Magnetic Droplets on Superhydrophobic Surfaces

Jaakko V. I. Timonen,[1]*† Mika Latikka,[1] Ludwik Leibler,[2] Robin H. A. Ras,[1]* Olli Ikkala[1]*

Self-assembly is a process in which interacting bodies are autonomously driven into ordered structures. Static structures such as crystals often form through simple energy minimization, whereas dynamic ones require continuous energy input to grow and sustain. Dynamic systems are ubiquitous in nature and biology but have proven challenging to understand and engineer. Here, we bridge the gap from static to dynamic self-assembly by introducing a model system based on ferrofluid droplets on superhydrophobic surfaces. The droplets self-assemble under a static external magnetic field into simple patterns that can be switched to complicated dynamic dissipative structures by applying a time-varying magnetic field. The transition between the static and dynamic patterns involves kinetic trapping and shows complexity that can be directly visualized.

Functional patterns and structures are essential in a wide variety of natural and engineered systems (*1*). They often form of small subunits by autonomous self-assembly, which is driven by free-energy gradients (*2*). Static self-assembly denotes a process in which the system reaches an energy minimum (equilibrium) wherein the ordered structure appears. Archetypical examples are structured block copolymers (*3*, *4*), nanoparticles (*5*, *6*), nanorods (*7*), liquid crystals (*8*), and hierarchical supramolecular systems (*9*). They find applications in data storage (*10*) and structural colors (*11*), for instance. On the other hand, dynamic self-assembly denotes a process in which the structure forms when the system is forcefully kept away from an energy minimum (out of equilibrium) by continuous energy supply and dissipation (*12*, *13*). Dynamic self-assembly is most notably encountered in biological systems (*14*–*16*),

[1]Department of Applied Physics, Aalto University (formerly Helsinki University of Technology), P.O. Box 15100, FI-02150 Espoo, Finland. [2]Matière Molle et Chimie, UMR 7167 CNRS-ESPCI, Ecole Supérieure de Physique et Chimie Industrielles, 10 rue Vauquelin, 75005 Paris, France.

*Corresponding author. E-mail: jaakko.timonen@aalto.fi (J.V.I.T.); robin.ras@aalto.fi (R.H.A.R.); olli.ikkala@aalto.fi (O.I.)
†Present address: Non-Equilibrium Energy Research Center, Northwestern University, 2145 Sheridan Road, Evanston, IL 60208, USA.

but seminal works have shown that it can also be created artificially (*12*, *13*, *17*).

Dynamic self-assembly has been suggested as a route to adaptive systems beyond what static self-assembly can offer (*2*, *13*, *18*). However, dynamic assembly is challenging to realize and understand because it cannot be predicted through energy minimization. It is also sensitive to small, local changes in the interactions between the elementary units and the external energy supply (*13*). We approach this problem by introducing a model system that functions in the interface of static and dynamic self-assembly and can be switched between them. The system relies on manipulation of mobile magnetic ferrofluid droplets (*19*–*21*) on a low-friction lotus-leaf–like (*22*) superhydrophobic surface (*23*–*27*) with an external magnetic field. In the following text, we first show how an external magnetic trigger can be used for creating self-assembled ferrofluid droplet populations from a single parent droplet. Then, we demonstrate that the static equilibrium patterns can be transformed reversibly to dynamic dissipative patterns by feeding them energy through

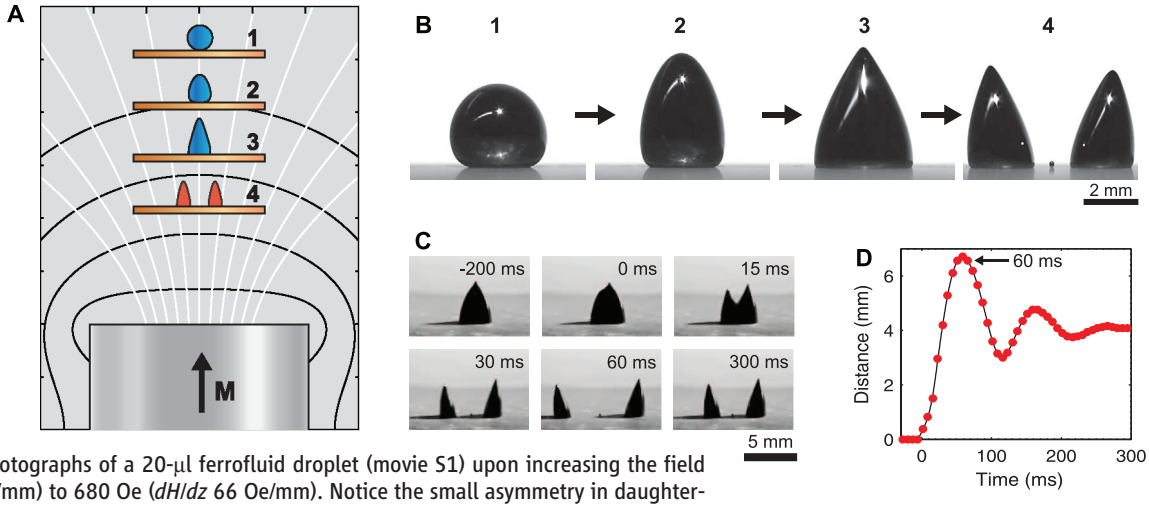

Fig. 1. Magnetically triggered ferrofluid droplet division on a superhydrophobic surface. (**A**) Schematic side-view of the magnetic field geometry of a cylindrical permanent magnet (white lines, magnetic field; black lines, constant field contours). State of the droplet is indicated as follows: 1, near-zero field (nearly spherical droplet); 2, weak field (slightly deformed droplet); 3, strong field (conical spiked droplet); and 4, above critical field (two daughter droplets). (**B**) Photographs of a 20-μl ferrofluid droplet (movie S1) upon increasing the field from 80 Oe (*dH/dz* 3.5 Oe/mm) to 680 Oe (*dH/dz* 66 Oe/mm). Notice the small asymmetry in daughter-droplet sizes and the small satellite droplet between the two (fig. S3). (**C**) Frames of a high-speed video of the division (movie S2) and (**D**) the corresponding distance between the daughter droplets as a function of time, approaching the distance determined by static self-assembly.

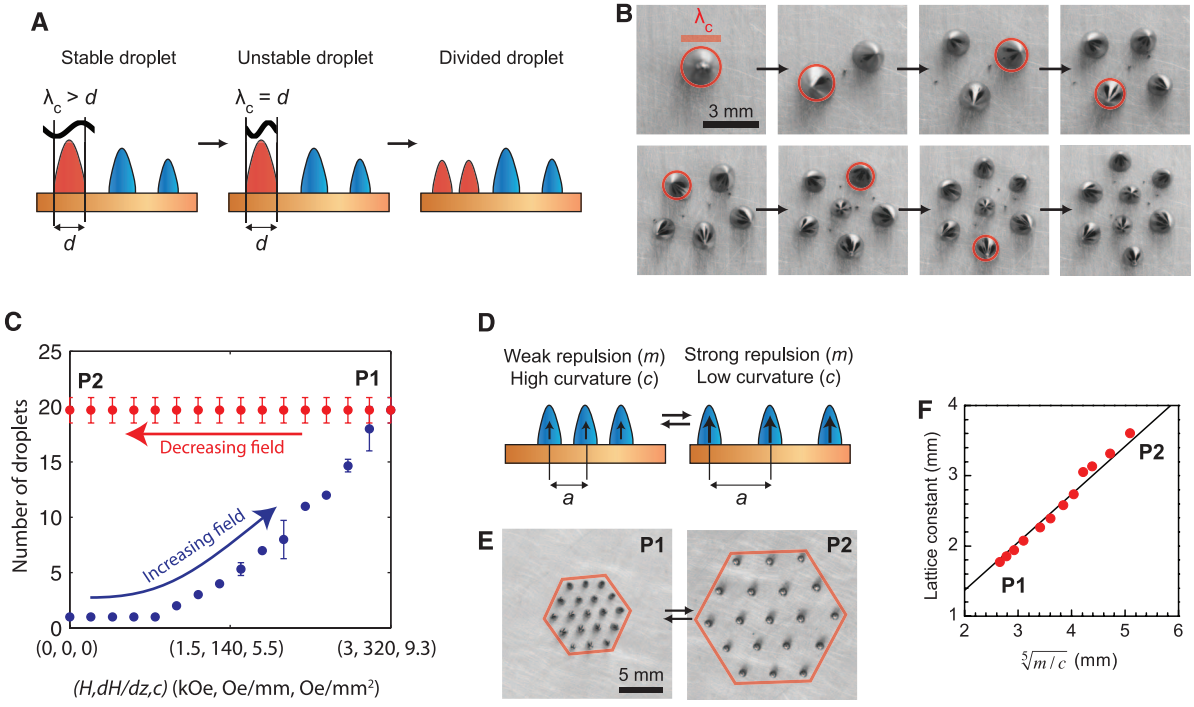

Fig. 2. Self-assembled droplet patterns in axisymmetric magnetic field. (**A**) Scheme of the division instability. λ_c, critical wavelength; d, diameter. (**B**) Photographs of the stepwise division and self-assembly of a 10-μl droplet. The largest droplet marked with a red circle (the diameter corresponds to λ_c; see Eq. 1) divides in each step (movie S3). Magnetic field strength was increased from 1.0 kOe (*dH/dz* 82 Oe/mm) for one droplet to 1.9 kOe (*dH/dz* 193 Oe/mm) for eight droplets. (**C**) Number of droplets as a function of increasing and decreasing magnetic field, showing hysteresis due to the kinetic trapping. P1; high magnetic field; P2, low magnetic field. Error bars indicate SD of three data sets. (**D**) Scheme of controlling the lattice constant in the kinetically trapped patterns by adjusting the magnetic field curvature (*c*) and the magnetic moment of the droplets (*m*). a, nearest-neighbor distance. (**E**) Snapshots of a 19-droplet pattern with two extreme periodicities at high and low magnetic fields. (**F**) The corresponding nearest-neighbor distance as a function of $\sqrt[5]{m/c}$. Red dots denote experimental measurements; the black line indicates the best linear fit.

an oscillating magnetic field. We highlight the important role of kinetic trapping as a stabilizer on both static and dynamic patterns and directly visualize the complexity of the transition.

In an elementary experiment, one droplet of aqueous ferrofluid (fig. S1) (*28*) is placed on a superhydrophobic surface and subjected to a confining field of a cylindrical permanent magnet below the substrate (Fig. 1A and fig. S2). Gradually increasing the field strength H and the vertical gradient dH/dz acting on the droplet (by decreasing the gap between the magnet and the surface) leads to a deformation of the droplet into a spiked cone and cleavage into two smaller droplets at the critical field strength (Fig. 1B and movie S1). The division takes a few tens of milliseconds (Fig. 1C and movie S2), after which the daughter droplets briefly oscillate before settling at their equilibrium separation (Fig. 1D).

The division of the droplet is due to a combination of high magnetic field and high vertical magnetic field gradient and, therefore, does not take place in a homogeneous magnetic field (fig. S4). The division is related to the normal-field instability of ferrofluids (Rosensweig instability) (*19*), but differs from it in several ways. The classic Rosensweig pattern [see (*29*) for a demonstration] appears in a homogeneous perpendicular magnetic field on a horizontal flat surface of ferrofluid. It has the critical periodicity of $\lambda_c^{\text{Rosensweig}} = 2\pi\sqrt{\sigma/\rho g}$, where σ and ρ are surface tension and density of the fluid, respectively, and g is the gravitational acceleration (*30*). In contrast, the gravitational force in our system is negligible compared with the magnetic force due to the vertical field gradient; that is, $\frac{d}{dz}(\mu_0 HMV)$, where μ_0 is permeability of vacuum, M is magnetization, and V is volume of the droplet. This magnetic force can be up to two orders of magnitude larger than the gravitational force (fig. S5). Thus, we can approximate the critical wavelength in our system as

$$\lambda_c \approx 2\pi\sqrt{\frac{\sigma}{\frac{d}{dz}(\mu_0 HM)}} \qquad (1)$$

Importantly, Eq. 1 has a different interpretation compared with the Rosensweig pattern. In this case, Eq. 1 does not determine the periodicity of the pattern but instead gives the criterion for the splitting: a droplet divides when the critical wavelength becomes smaller than the droplet diameter. This implies that the largest droplet is always the most susceptible to dividing (Fig. 2A), which was experimentally confirmed when the magnetic field was increased to generate larger droplet populations (Fig. 2B and movie S3), up to 75 droplets (fig. S6). In further contrast, the Rosensweig pattern is reversible (the pattern decays when the field is removed), but our patterns are not: the droplets do not coalesce back to a single droplet when the static magnetic field is switched off (Fig. 2C and movie S3). This irreversibility is due to the daughter droplets being kinetically trapped to remain separate; that is, there is a potential energy barrier between the global one-droplet energy minimum and any multidroplet pattern. The kinetic trapping is caused by the magnetic repulsion of the droplets and the nonwetting nature of the substrate (which ensures that the droplets are not physically connected). Later, we show a route back to the original one-droplet state through dynamic self-assembly.

The droplet pattern quickly rearranges to accommodate the newly formed droplet after each division (Fig. 2B and movie S3). The rearrangement is driven by the minimization of energy, which is a sum of the dipolar repulsion between the magnetized droplets and their attraction toward the increasing gradient of the external magnetic field

$$U = \frac{\mu_0}{4\pi}\sum_{i=1}^{N}\sum_{j=i+1}^{N}\frac{m_i m_j}{|\mathbf{r}_i - \mathbf{r}_j|^3} - \mu_0\sum_{i=1}^{N} m_i\left(H - \frac{1}{2}c|\mathbf{r}_i|^2\right) \qquad (2)$$

where m_i and m_j are magnetic moments of the droplets; $\mathbf{r}_i$ and $\mathbf{r}_j$ are positions of the droplets; and $c = -\frac{d^2H}{dr^2}$ is the confining curvature of the

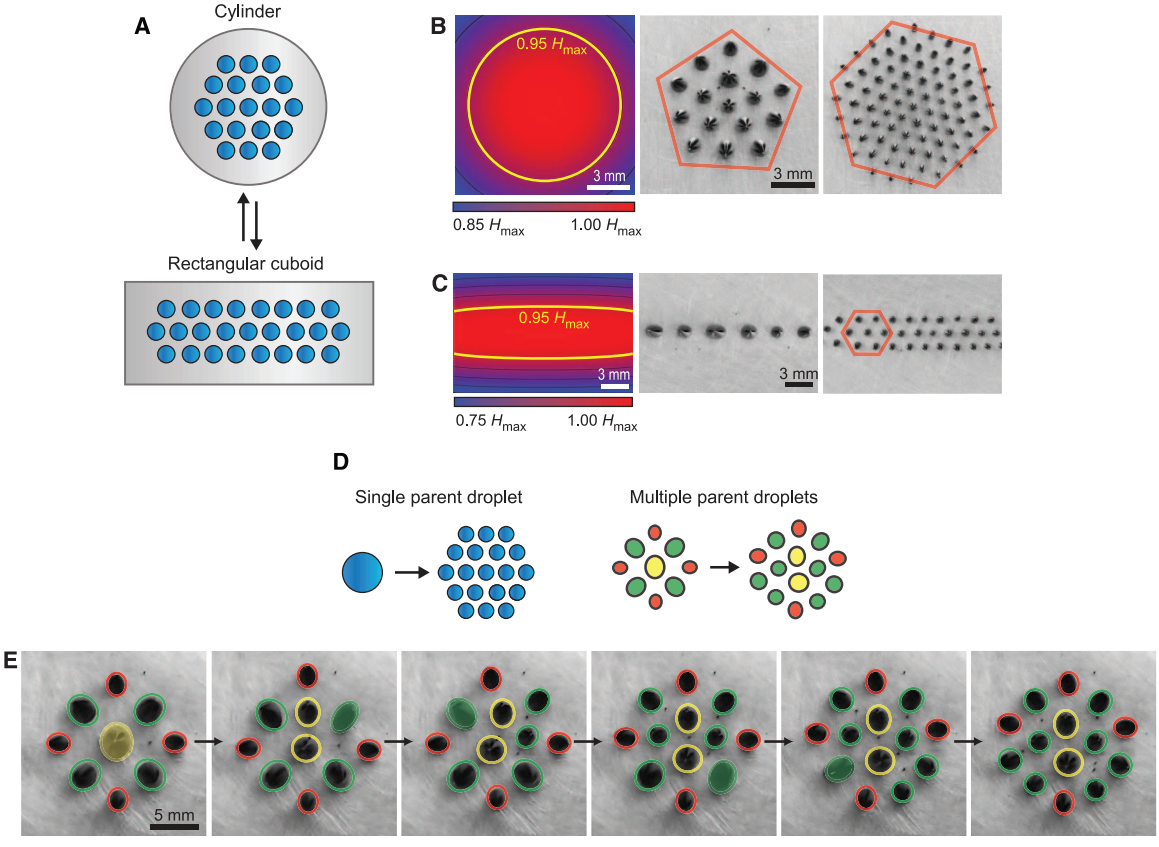

Fig. 3. More complicated patterns. (**A**) Scheme of changing the geometry of the magnetic field (top view). (**B**) Axisymmetric magnetic field (cylindrical magnet) and the corresponding patterns with five- and sixfold symmetries and (**C**) nonaxisymmetric magnetic field (rectangular cuboid magnet) and the corresponding close-packed ribbon patterns with an overall twofold symmetry (movie S5). All four patterns in (B) and (C) were created from a single 20-μl parent droplet. H_{max}, maximum magnetic field strength. (**D**) Scheme for changing the number of parent droplets. (**E**) An example of switching a hierarchical pattern of 9 droplets with fourfold symmetry with three droplet sizes to another hierarchical pattern of 14 droplets with twofold symmetry (movie S6). The dividing droplet is marked with a solid color. The magnetic field strength was increased from 1060 Oe (*dH/dz* 61 Oe/mm) to 1240 Oe (*dH/dz* 72 Oe/mm).

magnetic field (fig. S2). The rearrangement after each division is nearly perfect due to the low friction that originates from the surface's high contact angles and low contact angle hysteresis. In contrast, other surfaces with higher contact angle hysteresis did not allow the minimum energy patterns to be reached (movie S4).

The lattice constant of the patterns could be adjusted by changing the ratio between the repulsion and attraction by changing the distance between the surface and the magnet (Fig. 2, D to F), in good agreement with the scaling relation for the nearest-neighbor distance $a \propto \sqrt[5]{m/c}$ predicted from Eq. 2. Importantly, the periodicity changes are completely reversible (provided that the field is not increased above the next division threshold). Thus, the droplets are free to move, despite the number of droplets being kinetically trapped (Fig. 2C).

More complicated patterns are readily achieved by using other magnetic field geometries, such as that of a nonaxisymmetric rectangular cuboid magnet (Fig. 3A). The lacking axial symmetry changes the typical five- and sixfold patterns observed with cylindrical magnets (Fig. 3B) to close-packed ribbons with an overall twofold symmetry (Fig. 3C and movie S5). On the other hand, starting with multiple differently sized parent droplets (Fig. 3D) makes switching between hierarchical patterns possible (Fig. 3E, fig. S7, and movie S6).

The static patterns transform to dynamic ones when they are provided with a sufficient continuous energy feed to keep them away from the energy minimum (Fig. 4A). We realized the energy feed by oscillating the permanent magnet horizontally below the substrate with amplitude A and frequency f (Fig. 4B). At low energy feed rates (small amplitude and frequency), a typical static seven-droplet pattern simply moves with the oscillating magnet as a whole and, thus, remains close to the energy minimum (Fig. 4, C and D, mode I, and movie S7). However, the droplets start to coalesce above a threshold amplitude and frequency, leading to the emergence of numerous dynamic patterns consisting of elongated droplets and/or regular circular droplets (Fig. 4, D and E, modes II to X, and movies S7 and S8). The transition threshold is determined by the time-dependent dissipative magnetic forces, which cause shortening in the distances between the droplets (fig. S8). Thus, the dynamic magnetic force is an external trigger that can free the static pattern from its kinetic trap (Fig. 2C). It allows the number and sizes of the droplets to be changed, leading to the rearrangement of the pattern.

Simulations showed that the coalescence and rearrangement starts from droplet pairs whose distance is affected the most by the energy feed (Fig. 4F and fig. S8). However, immediately after the first coalescence, the behavior of the pattern becomes difficult to predict, as seen from the complex and seemingly chaotic coalescence and division of droplets (movie S8, mode IX). This complexity originates mostly from small differences in initial positions and sizes of the droplets (fig. S6). However, complexity can arise, even in individually pipetted droplet patterns (movie S10), and is actually seen also in switching of some static patterns (fig. S9 and movie S11). Yet, even the most chaotic transient droplet motions eventually stabilize into kinetically trapped patterns that are permanent until the oscillating field is switched off, after which the

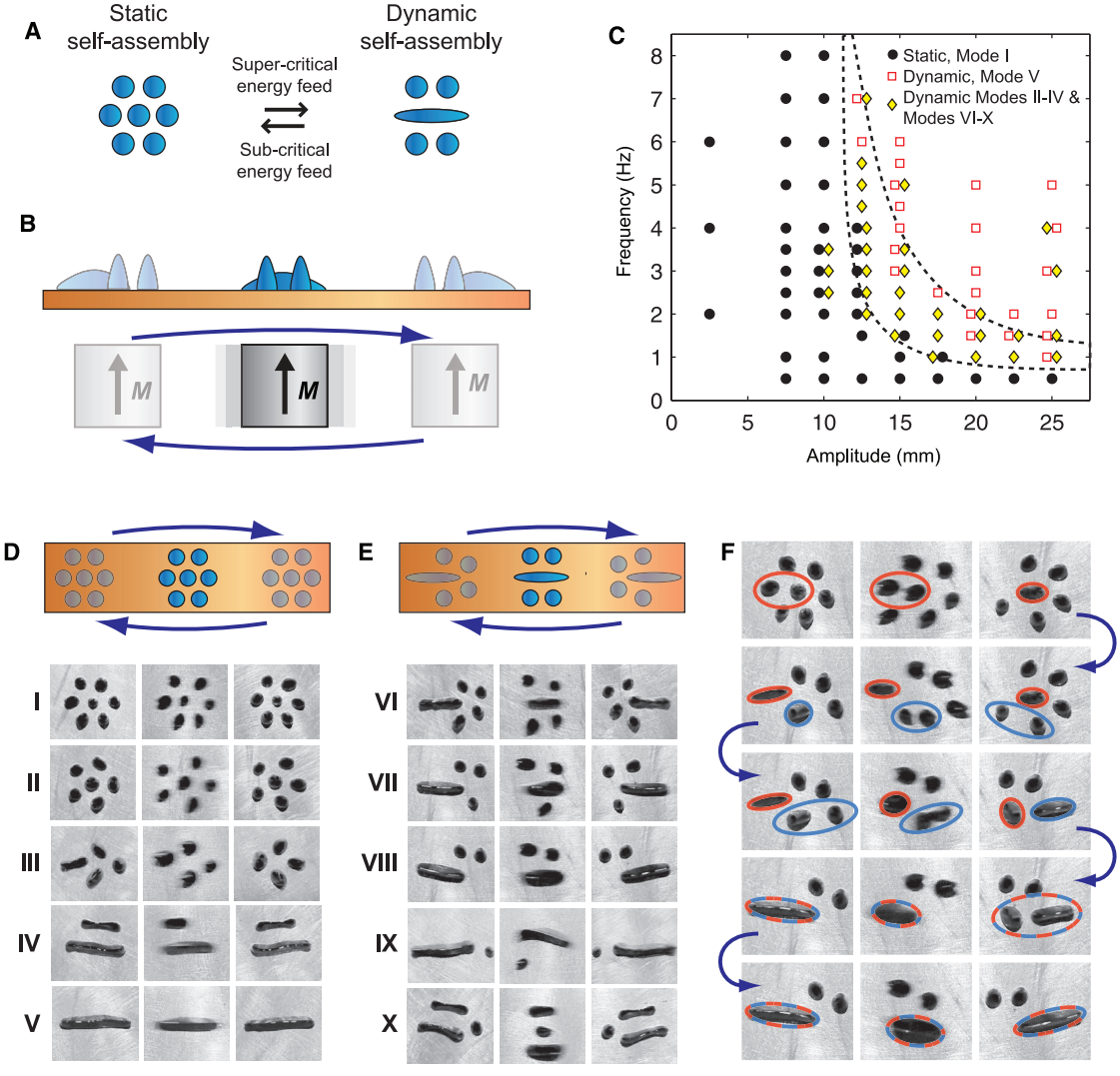

Fig. 4. Reversible switching between static and dynamic self-assembly. (**A**) Scheme of the switching. (**B**) Practical realization of the energy feed by horizontally oscillating the permanent magnet below the superhydrophobic surface. (**C**) Phase diagram of the seven-droplet pattern in the field of 1130 Oe (dH/dz 132 Oe/mm), showing the transition boundary (dashed lines). (**D**) Scheme of mode I and photographs of dynamic patterns that do not change their appearance during the cycle of the driving field (movie S7). (**E**) Scheme of mode VI and photographs of dynamic patterns that change their shape (but not the number of droplets) periodically with the external magnetic field (movie S8). (**F**) Photographs of the intermediate steps in the formation of mode VIII during 2.5 oscillations of the driving field (f = 3 Hz, A = 12.5 mm) (movie S9).

patterns decay back to the static seven-droplet pattern within a fraction of a second.

Dynamic patterns rely critically on low friction and energy dissipation (movie S12). The geometry of the dynamic patterns cannot be described in terms of energy minimization (Eq. 2), because they are far from the energy minimum. Instead, the patterns are better described and rationalized as dynamic states wherein the droplet number is kinetically trapped [as in the static patterns (Fig. 2C)]. Patterns can be classified into those that alternate (Fig. 4E) or do not alternate (Fig. 4D) during the cycled energy feed. Alternation is caused by different mobilities of the droplets: Elongated ones are more mobile because of the higher ratio between the driving and dissipative forces.

Dynamic self-assembly can be used as a switch between droplet patterns with different numbers of droplets. In contrast to the division instability, dynamic self-assembly decreases the number of droplets. This allows the irreversibility of the droplet formation in static self-assembly (Fig. 2C) to be overcome. For example, driving any static pattern to the mode V dynamic pattern (single elongated droplet) and decreasing the magnetic field while oscillating the magnet allows recovery of the original one-droplet state (movie S13). This is the final unit operation required to realize a complete cycle from a single liquid droplet to complicated static and dynamic patterns and, finally, back to the starting state (fig. S10).

Externally driven magnetic droplets on superhydrophobic surfaces form a versatile model system for studying and visualizing complicated phenomena in self-assembly. We used this model to demonstrate switching between static and dynamic self-assembly and to show the usefulness of kinetic trapping that most often is viewed only as a hindrance for assembly. The most diverse patterns were found to occur near the boundary where static patterns switch to dynamic ones. The transition is complex, and its detailed investigations will pave the way toward a better understanding of the onset of dynamic dissipative self-assembly.

References and Notes

1. P. Ball, *Nature's Patterns: A Tapestry In Three Parts* (Oxford Univ. Press, Oxford, 2011).
2. G. M. Whitesides, B. Grzybowski, *Science* **295**, 2418–2421 (2002).
3. F. S. Bates *et al*., *Science* **336**, 434–440 (2012).
4. A.-V. Ruzette, L. Leibler, *Nat. Mater.* **4**, 19–31 (2005).
5. Y. Xia *et al*., *Nat. Nanotechnol.* **6**, 580–587 (2011).
6. E. V. Shevchenko, D. V. Talapin, N. A. Kotov, S. O'Brien, C. B. Murray, *Nature* **439**, 55–59 (2006).
7. K. Liu, N. Zhao, E. Kumacheva, *Chem. Soc. Rev.* **40**, 656–671 (2011).
8. T. Kato, N. Mizoshita, K. Kishimoto, *Angew. Chem. Int. Ed.* **45**, 38–68 (2006).
9. O. Ikkala, G. ten Brinke, *Science* **295**, 2407–2409 (2002).
10. S. Park *et al*., *Science* **323**, 1030–1033 (2009).
11. J. Yoon, W. Lee, E. L. Thomas, *MRS Bull.* **30**, 721–726 (2005).
12. B. A. Grzybowski, C. J. Campbell, *Chem. Eng. Sci.* **59**, 1667–1676 (2004).
13. B. A. Grzybowski, C. E. Wilmer, J. Kim, K. P. Browne, K. J. M. Bishop, *Soft Matter* **5**, 1110–1128 (2009).
14. S. Kauffman, *At Home in the Universe: The Search for Laws of Self-Organization and Complexity* (Oxford Univ. Press, Oxford, 1995).
15. E. Karsenti, *Nat. Rev. Mol. Cell Biol.* **9**, 255–262 (2008).
16. A. M. Mateus, N. Gorfinkiel, A. M. Arias, *Semin. Cell Dev. Biol.* **20**, 877–884 (2009).
17. B. A. Grzybowski, H. A. Stone, G. M. Whitesides, *Nature* **405**, 1033–1036 (2000).
18. K. V. Tretiakov, K. J. M. Bishop, B. A. Grzybowski, *Soft Matter* **5**, 1279–1284 (2009).
19. R. E. Rosensweig, *Ferrohydrodynamics* (Dover Publications, New York, 1997).
20. J.-C. Bacri, F. Elias, in *Morphogenesis: Origins of Patterns and Shapes*, P. Bourgine, A. Lesne, Eds. (Springer, Heidelberg, 2011), pp. 15–19.
21. R. Massart, *IEEE Trans. Magn.* **17**, 1247–1248 (1981).
22. W. Barthlott, C. Neinhuis, *Planta* **202**, 1–8 (1997).
23. I. A. Larmour, S. E. J. Bell, G. C. Saunders, *Angew. Chem. Int. Ed.* **46**, 1710–1712 (2007).
24. X. F. Gao *et al*., *Adv. Mater.* **19**, 2213–2217 (2007).
25. H. Mertaniemi *et al*., *Adv. Mater.* **23**, 2911–2914 (2011).
26. H. Mertaniemi, R. Forchheimer, O. Ikkala, R. H. A. Ras, *Adv. Mater.* **24**, 5738–5743 (2012).
27. T. Verho *et al*., *Proc. Natl. Acad. Sci. U.S.A.* **109**, 10210–10213 (2012).
28. R. Massart, E. Dubois, V. Cabuil, E. Hasmonay, *J. Magn. Magn. Mater.* **149**, 1–5 (1995).
29. D. Castelvecchi, *Phys. Rev. Focus* **15**, 18 (2005).
30. B. Berkovsky, V. Bashtovoi, *IEEE Trans. Magn.* **16**, 288–297 (1980).

Acknowledgments: We acknowledge financial support from the National Doctoral Programme in Materials Physics, Nokia Research Center, the Academy of Finland, a European Research Council Advanced Grant, and the Finnish Agency of Technology and Innovation (TEKES). Electron microscopy was performed using the devices of the Nanomicroscopy Center of Aalto University. We thank A. Walther (RWTH Aachen University), A. Kuzyk, and M. Kostiainen for comments on the manuscript and T. Huhtamäki and J. Korhonen for preparing the silicone nanofilament surfaces.

Supplementary Materials

www.sciencemag.org/cgi/content/full/341/6143/253/DC1
Materials and Methods
Supplementary Text
Figs. S1 to S10
References (*31*–*35*)
Movies S1 to S14

7 December 2012; accepted 10 June 2013
10.1126/science.1233775

Ultrahigh Magnetoresistance at Room Temperature in Molecular Wires

R. N. Mahato,[1] H. Lülf,[2] M. H. Siekman,[1,3] S. P. Kersten,[4] P. A. Bobbert,[4] M. P. de Jong,[1] L. De Cola,[2,5] W. G. van der Wiel[1]*

Systems featuring large magnetoresistance (MR) at room temperature and in small magnetic fields are attractive owing to their potential for applications in magnetic field sensing and data storage. Usually, the magnetic properties of materials are exploited to achieve large MR effects. Here, we report on an exceptionally large (>2000%), room-temperature, small-field (a few millitesla) MR effect in one-dimensional, nonmagnetic systems formed by molecular wires embedded in a zeolite host crystal. This ultrahigh MR effect is ascribed to spin blockade in one-dimensional electron transport. Its generic nature offers very good perspectives to exploit the effect in a wide range of low-dimensional systems.

In spintronic devices, the electron's spin is exploited for information processing. Typically, these devices contain layered structures with an electrical resistance that is dependent on the relative orientation of the magnetization of their magnetic layers; thus, the resistance can be altered by an external magnetic field, a phenomenon called magnetoresistance (MR). Examples include giant magnetoresistance (GMR) devices (*1*, *2*), which are multilayer stacks of ferromagnetic materials separated by a nonmagnetic metal spacer layer, and tunnel magnetoresistance (TMR) devices (*3*, *4*), which have a tunnel barrier as the spacer. Here, we explore entirely different physics in a nonmagnetic system, relying on a mechanism akin to spin blockade in quantum devices.

The Pauli principle precludes that an electron can tunnel into a state already occupied by another electron with the same spin. This spin blockade for two electrons starting from a spin-triplet configuration was first observed in quantum dots (QDs) at cryogenic temperatures (*5*). Spin blockade can be lifted by spin relaxation, mixing in singlet character. It has been shown that hyperfine interaction can lift spin blockade in QDs (*6*). The importance of hyperfine interaction on spin dynamics has also been recognized in the context of an intrinsic, room-temperature MR effect in organic semiconductors (*7*, *8*). Carrier transport is influenced by spin-dependent reactions, which are subject to the competition between an external magnetic field B and the random hyperfine fields B_{hf} (~1 mT) of the nuclei. At small B (Fig. 1A), hyperfine interactions

[1]NanoElectronics Group, MESA+ Institute for Nanotechnology, University of Twente, P.O. Box 217, 7500 AE, Enschede, Netherlands. [2]Institut de Science et d'Ingénierie Supramoléculaires (ISIS), Université de Strasbourg, 8 Allée Gaspard Monge, 67000 Strasbourg, France. [3]Transducers Science and Technology Group, MESA+ Institute for Nanotechnology, University of Twente, P.O. Box 217, 7500AE Enschede, Netherlands. [4]Theory of Polymers and Soft Matter, Department of Applied Physics, Eindhoven University of Technology, P.O. Box 513, 5600 MB, Eindhoven, Netherlands. [5]Karlsruher Institut für Technologie (KIT), Institut für Nanotechnologie Hermann-von-Helmholtz-Platz 1, D-76344 Eggenstein-Leopoldshafen, Germany.

*Corresponding author. E-mail: w.g.vanderwiel@utwente.nl

Switchable Static and Dynamic Self-Assembly of Magnetic Droplets on Superhydrophobic Surfaces

Jaakko V. I. Timonen *et al.*

Science **341**, 253 (2013);
DOI: 10.1126/science.1233775